Lithium Niobate Electro-Optic Racetrack Modulator Etched in Y-Cut LNOI Platform

Volume 10, Number 1, February 2018

Mohamed Mahmoud
Lutong Cai
Christian Bottenfield
Gianluca Piazza

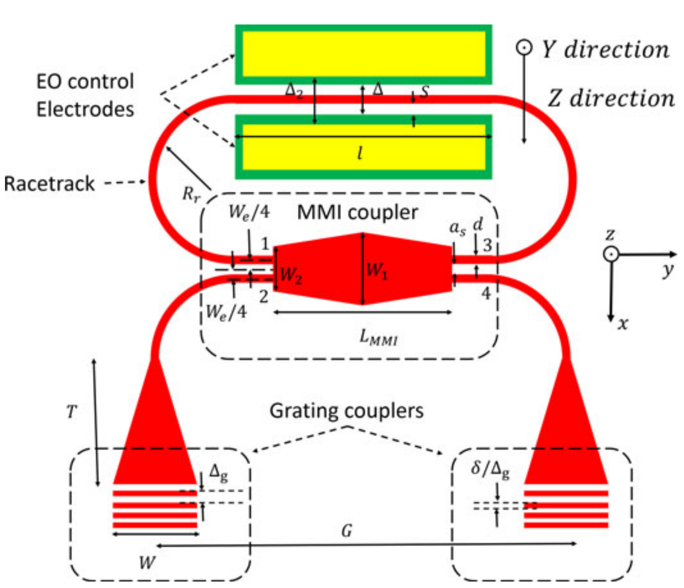

DOI: 10.1109/JPHOT.2018.2797244
1943-0655 © 2018 IEEE

Lithium Niobate Electro-Optic Racetrack Modulator Etched in Y-Cut LNOI Platform

Mohamed Mahmoud, Lutong Cai, Christian Bottenfield, and Gianluca Piazza

Department of Electrical and Computer Engineering, Carnegie Mellon University, Pittsburgh, PA 15213 USA

DOI:10.1109/JPHOT.2018.2797244
1943-0655 © 2018 IEEE.Translations and content mining are permitted for academic research only. Personal use is also permitted, but republication/redistribution requires IEEE permission. See http://www.ieee.org/publications_standards/publications/rights/index.html for more information.

Manuscript received December 14, 2017; revised January 15, 2018; accepted January 18, 2018. Date of publication January 30, 2018; date of current version February 7, 2018. This work supported by the DARPA PRIGM-AIMS program under Award No. N66001-16-1-4025. Corresponding author: Mohamed Mahmoud (e-mail: mohamed85mahmoud85@gmail.com).

Abstract: An electro-optic modulator (EOM) based on a racetrack resonator coupled to a waveguide using butterfly multi-mode interference (MMI) coupler is fabricated on Y-cut lithium niobate (LN) thin film. This is the first demonstration of a LN EOM in which the thin film of LN is etched in a Y-cut substrate using chlorine-based inductively coupled plasma reactive ion etching, a process, which is readily compatible with semiconductor fabrication facility. The Y-cut LNOI platform is interesting for the integration of electro-optic and acousto-optic components, since differently from any other LN cut it facilitates taking advantage of the maximum electro-optic and piezoelectric coefficients of LN. Coupling to the racetrack was enabled using a butterfly MMI coupler, which offered operation near the critical coupling condition, hence increasing the extinction ratio (ER) of the modulator. An unloaded quality factor of 1.3×10^5 was extracted for this device, which is equivalent to a propagation loss of 2.3 dB/cm. Modulation bandwidth of 4 GHz, wavelength tuning rate of 0.32 pm/V, and an ER of more than 10 dB were experimentally measured for the EOM.

Index Terms: Lithium niobate, integrated optics materials, electro-optical devices.

1. Introduction

Ring or racetrack resonators are important building blocks in integrated optics and very promising in applications including wavelength-division-multiplexing (WDM), cavity quantum electrodynamics (cavity QED), opto-mechanics and high sensitivity sensors [1]–[4]. Electro-optical (E-O) tunable racetrack resonators are of particular interest as they can efficiently modulate the photonic signal and work as building blocks of complex and reconfigurable photonic networks [5]. Silicon E-O modulators (EOMs) have been heavily investigated, but the intrinsic lack of electro-optical property in Silicon limits its performance [6], [7], [8]. On the other hand, the intrinsic strong electro-optic effect of lithium niobate (LN) makes such material an ideal platform for fabricating E-O modulators and nonlinear photonic devices [9]–[12]. However, conventional LN waveguides built using Ti diffusion or proton exchange suffer from low index-contrast, leading to low optical confinement, large footprint, and the need for higher modulation voltages [13]–[15]. To attain better optical confinement, various research groups have investigated the use of the high index contrast provided by the Lithium Niobate on Insulator (LNOI) platform [5], [11], [12], [16]–[22]. Various techniques for etching LN including ion milling, ion-beam-enhanced etching, and focused ion beam [18], [19], [23] were explored and yielded functional devices, but are not readily scalable to large substrates and production environments.

Other groups avoided all together etching the LN by using LN as an active layer on top of a Si waveguide [24], [25] or used a loaded strip of different material that has an index of refraction similar to LN and placed it above LN to build the core of the waveguide [20]. More recent work [26] has shown a reliable process for etching LN using Argon plasma reactive ion etching (RIE) and demonstrated high speed optical modulation for devices built on X-cut LNOI wafers. This recent work was the first of its kind. Our lab has previously investigated reactive etching of LN using Chlorine (Cl_2) based chemistry to build acoustic resonators [27]. This article represents the first exploration of this technique to build photonic components. Integrating the electrodes with the LN etch enabled building EOM in a Y-cut LNOI substrate. Y-cut LN offers unique capabilities as it facilitates the use of both high electro-optic and acousto-optic/piezoelectric coefficients intrinsic to this specific cut [28]. Thus, etching optical waveguides that can efficiently confine the propagating light and integrating electrodes in the same process on Y-cut LN sets a pathway for the synthesis of various building blocks needed in high-speed communication links. In Y-cut LN it is possible to simultaneously fabricate high performance electro-optic, acousto-optic and acoustic components. Herein, we demonstrate this fabrication process for Y-cut LN for realizing high speed EOMs based on a racetrack photonic resonator. To achieve a high extinction ratio in a racetrack resonator, the coupling ratio and the round trip loss must be matched so that the racetrack operates near the critical coupling point [29]. The operation near critical coupling point for a racetrack is also essential for phase sensing applications. For this purpose, a 2×2 MMI coupler was designed and fabricated in the LNOI platform. Rectangular MMI waveguides can only provide discrete coupling ratios (100/0 85/15 72/28 50/50). For that reason, a butterfly MMI coupler [30] was used, so that non-discrete coupling ratios could be obtained depending on the coupler geometry. This LNOI platform enabled the demonstration of a high Q racetrack resonators embedded in an EOM from which important information related to the material and device properties could be extracted: propagation losses of 2.3 dB/cm,a tuning rate of 0.32 pm/V, and modulation bandwidth of 4 GHz. Additionally, the demonstrated fabrication process and coupling method will permit to eventually control the coupling coefficient through the EO effect across the MMI coupler, hence further enhancing the tuning capabilities and robustness with respect to manufacturing variations of the proposed platform.

2. Theory of Operation and Design

Fig. 1 shows the proposed geometry for the E-O tunable racetrack resonator. The light is coupled in and out of the chip using grating couplers. Tapered waveguides are used as spot size converters from the wide waveguide at the gratings side to the narrow one that couples to the racetrack resonator. The MMI coupler is the coupling element to the racetrack resonator. The resonance wavelength is determined by the round trip phase shift inside the racetrack, which can be modified and tuned by the EO effect. The film stack is formed by a 1 μm thick silicon dioxide (SiO_2) ($n_c = 1.44$) film, which is used as a bottom cladding layer and a 500 nm thick layer of Y-cut LN, which is used as the active thin-film for the photonic devices. The two layers are placed on a LN carrier wafer (see fabrication section for more details on how the initial substrate was prepared). The grating design was optimized for maximum coupling at the wavelength, $\lambda = 1.55$ μm for TE polarization using Lumerical 2D FDTD tool. The optimization resulted in design values of $\Delta_g = 1$ μm for the pitch, $\delta/\Delta_g = 0.44$ for the duty cycle and $e = 330$ nm for the etch depth [21]. Both the gratings and the waveguides were defined in the same etch step and with the same etch depth to reduce the number of fabrication steps. The LN racetrack (red in Fig. 1) and the Aluminum electrodes (green in Fig. 1) were laid out such that the TE polarized light and the applied electric field are both parallel to the Z direction of the crystal to make use of the highest E-O coefficient, $r_{33} = 33$ pm/V. A Gold layer (yellow in Fig. 1) was also patterned on top of Al to facilitate the probing during device testing. The separation between the two couplers was set to match the separation in the V-groove fiber array used for measurements, $G = 250$ μm. The coupler waveguide width was set to $W = 17$ μm to facilitate the optical alignment of the single mode fiber (10 μm core). Single mode operation for LNOI rib-waveguides is allowed only for width $d \leq 0.8$ μm (see Fig. 2) at the selected etch depth. Given the constraints on the lithographic equipment used to define the waveguides, their width was

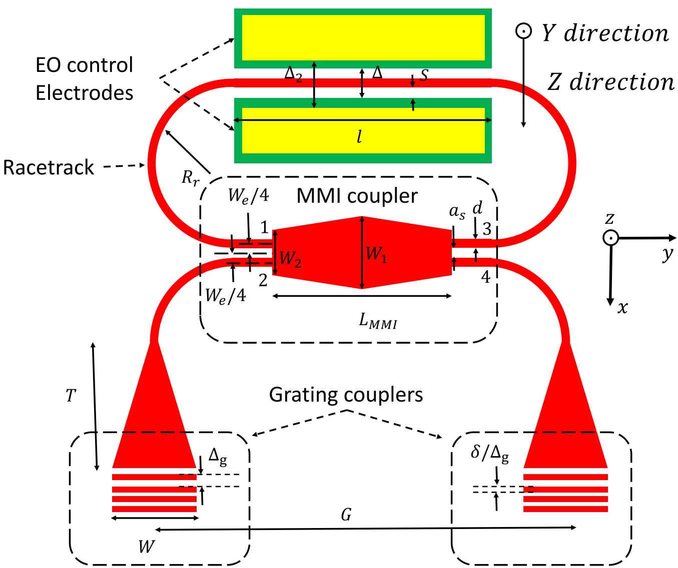

Fig. 1. Schematic view of the racetrack EOM. Grating couplers are used to couple in and out the light. The Butterfly MMI coupler is used to couple the light inside the racetrack resonator. The resonance condition dictated by the round trip phase shift inside the racetrack is altered by the applied electric field across the electrodes. The higher case symbols X, Y, Z refer to the material axis while the lower case ones x, y, z refer to the simulation axis.

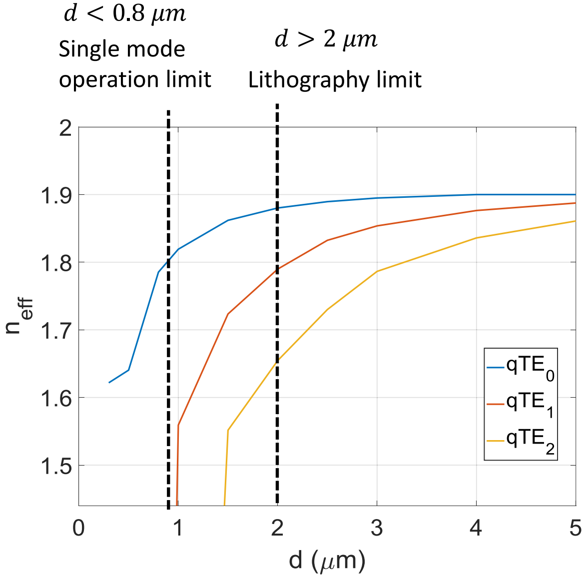

Fig. 2. Effective index of guided modes versus the waveguide width.

set to $d = 2$ μm. The length of the taper was set to $T = 700$ μm to minimize losses during spot size conversion.

The MMI coupler is used to couple light in and out of the racetrack resonator. It can be modeled as a 2×2 element with two input ports and two output ports such that the output fields, E_3 and E_4, at ports 3 and 4 are related to the input fields, E_1 and E_2, at ports 1 and 2 by the equations:

$$E_3 = re^{-j\phi_r}E_1 + te^{-j\phi_t}E_2 \tag{1}$$

$$E_4 = te^{-j\phi_t}E_1 + re^{-j\phi_r}E_2 \tag{2}$$

Where r and t are the electric field amplitude coupling coefficients for the direct and cross waveguides respectively while ϕ_r and ϕ_t are the associated phase shifts. For a symmetric lossless coupler, the power conservation implies:

$$r^2 + t^2 = 1, \qquad \text{and} \qquad \phi_t = \phi_r - \pi/2 \tag{3}$$

Assuming that the propagation loss in the MMI coupler and the narrow waveguide is the same, and the field round trip loss inside the racetrack is given by $a = e^{-\alpha L_{RT}}$ where α is the loss per unit length and L_{RT} is the total equivalent length of the racetrack, the transfer function of the resonator can be derived with the help of Eq. (3) as:

$$T = \frac{a^2 + r^2 - 2ar\cos(\phi_l + \phi_r)}{1 + a^2 r^2 - 2ar\cos(\phi_l + \phi_r)} \tag{4}$$

where $\phi_l = n_{eff}\frac{2\pi}{\lambda}L_T$ is the phase shift due to propagation all the way around the loop except for the MMI coupler such that $L_T = 2l + 2\pi R_r - L_{MMI}$, $n_{eff} = 1.87$ is the effective index of the fundamental mode, $R_r = 100\ \mu$m is the radius of the curved section, $l = 500\ \mu$m is the length of the straight section as well as the electrodes length and L_{MMI} is the length of the MMI coupler. The critical coupling condition in the racetrack can be expressed as $r^2 = a^2$ and to get an ER larger than 10 dB, a coupling ratio larger than 80% is desired. For that purpose, a butterfly MMI coupler is used since rectangular MMI couplers can be designed only to get discrete and very specific splitting ratios ($r^2/t^2 = 0/100,\ 50/50,\ 72/28,\ 85/15$) [31]. Eigen Mode Expansion (EME) solver inside LUMERICAL tool was used to design the butterfly coupler. The analysis resulted in an MMI coupler with the dimensions, $W_1 = 10.67\ \mu$m as inner width, $W_2 = 7.46\ \mu$m as outer width and $L_{MMI} = 334.2\ \mu$m as coupler length for which a coupling coefficient of 83% was achieved.

The main parameter that guides the design of the racetrack EOM is the voltage tuning rate, which can be derived to be equal to:

$$TR \approx r_{33} n_{eff}^3 \frac{\lambda_{ro}}{2\Delta} \frac{l}{\left(n_{eff} L_T + n_{MMI} L_{MMI}\right)} \Gamma_{EO} \tag{5}$$

Where λ_{ro} is the resonance wavelength at zero voltage, $\Delta = d + 2S$ is the electrode separation, d is the waveguide width, S is the separation from the electrode to the waveguide, $n_{MMI} = 1.907$ is the effective index of the fundamental mode of the MMI waveguide, Γ_{EO} is the overlap between the optical field, $\varepsilon_{TE}(x, z)$, in the waveguide and the electrical field, $E_{0Z}(x, z)$, between the electrodes and is given by the equation:

$$\Gamma_{EO} = \frac{\Delta}{V} \frac{\int_{-\infty}^{\infty}\int_{-\infty}^{\infty} E_{0Z}(x, z)\,|\varepsilon_{TE}(x, z)|^2 dxdz}{\int_{-\infty}^{\infty}\int_{-\infty}^{\infty} |\varepsilon_{TE}(x, z)|^2 dxdz} \tag{6}$$

For obtaining maximum electric field and hence maximum tuning rate, a minimum separation between the electrodes should be selected. The minimum electrode to waveguide separation, $S_{\min}$, is dictated by the propagation losses introduced by the aluminum near the waveguide. LUMERICAL MODE solver was used to estimate the propagation loss, α, in dB/cm for the guided modes of the optical waveguide as a function of the separation distance, S. The only losses considered in the model were coming from the Al layer and modeled through an imaginary index of refraction. As shown in Fig. 3, an $S_{\min}$ of 2.6 μm reduces the losses due to the Al layer below 0.1 dB/cm. Note that this value can be reduced to $S_{\min} = 2\ \mu$m for a SM waveguide. Accordingly, the minimum separation between electrodes is $\Delta_{\min} = 4.8\ \mu$m for SM waveguide and $\Delta_{\min} = 7.2\ \mu$m for MM waveguide. However, in our design, Δ was conservatively chosen to be 12 μm to ensure no leakage of the optical mode in the aluminum layer.

To evaluate the expected TR, the optical and electric field were simulated respectively using LUMERICAL and COMSOL. The overlap between the two fields was evaluated using MATLAB (see Fig. 4) and the results for Γ_{EO} and TR are summarized in Table 1. This table shows the expected TR for our design and highlights how our proposed fabrication process could ultimately improve the TR if we were to use SM waveguides and minimize the electrode separation. Since

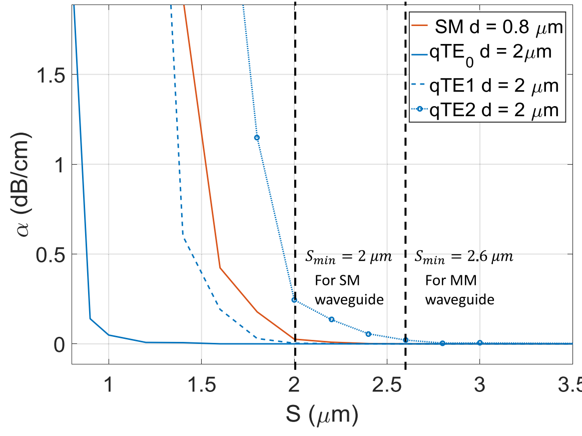

Fig. 3. Propagation loss of guided modes in dB/cm versus the separation distance between the waveguide and the aluminum metal electrodes.

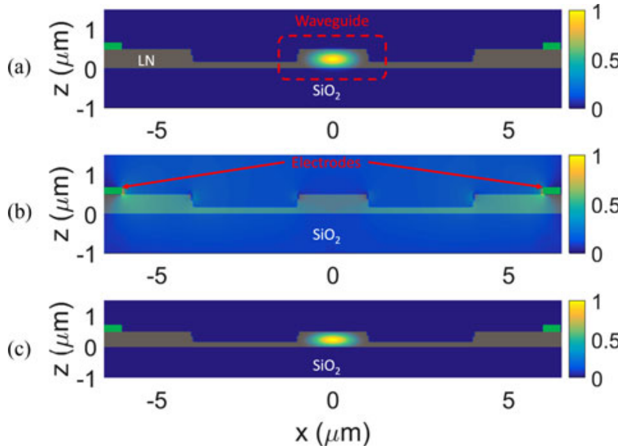

Fig. 4. a) Normalized optical field inside the waveguide. b) Normalized electric field c) Normalized product of the optical and electrical fields.

TABLE 1

Investigation of the Process Limitation on the EOM Performance for Possible Improvements

Description	$d(\mu m)$	$\Delta(\mu m)$	Γ_{EO}	*TR* (pm/V) for current electrode coverage length $l = 500\ \mu m$	*TR* (pm/V) for same racetrack but with maximum coverage ratio $l = 960\ \mu m$
MM (current design)	2	12	0.51	1.1	2
MM – (minimum Δ)	2	7.2	0.5	1.74	3.3
SM	0.8	4.8	0.49	2.2	4.3

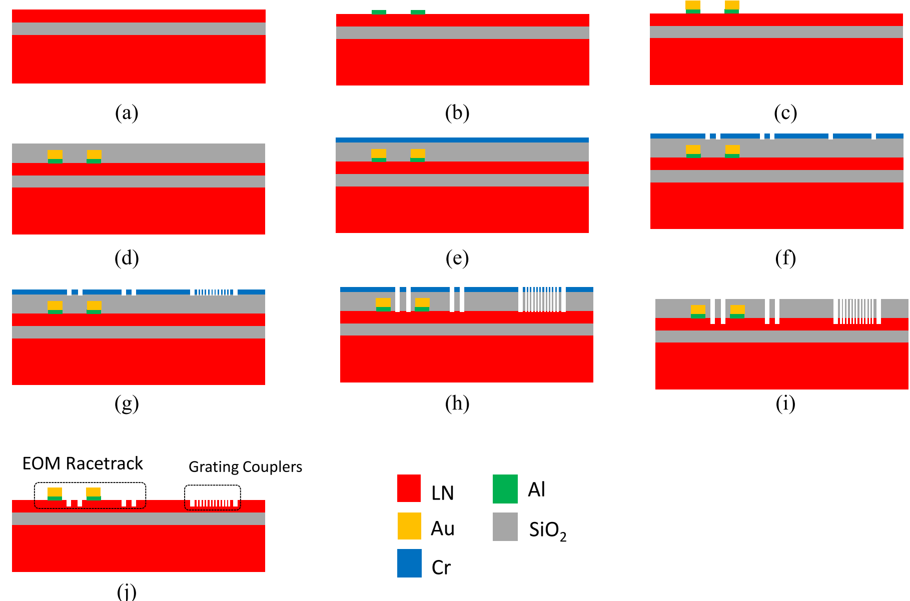

Fig. 5. Fabrication process flow for the RT EOM. a) LNOI substrate. b) Lift off of Al thin film to be used for the electrodes. c) Lift off of Au thin film which acts as coverage for Al film to facilitate wafer-level probing. d) Deposition of SiO_2, which is used as a LN etch mask. e) Deposition of Cr mask, which is used as SiO_2 etch mask f) Patterning of Cr using photo-lithography for defining WGs. g) Patterning of Cr using electron-beam lithography for gratings coupler definition. h) Etching SiO_2 in Fluorine-based chemistry. i) Etching of LN in Chlorine-based chemistry. j) Wet etch of SiO_2 using Al PAD etch.

the *TR* increases linearly with the metal coverage ratio, l/L_T, the *TR* should double when we use the maximum coverage ratio. The overlap factor Γ_{EO} is about 50% in all the cases considered in this study. As shown in Fig. 4, the LN etch allows confining most of the optical power in the LN core which is the EO active material. The overlap factor is still limited by the spatial distribution of the electric field that depends on the ratio between the dielectric constant of LN and air. Using another cladding material like SiO_2 would have helped better confining the electric field in the LN and improve that factor [19].

3. Fabrication and Measurement

The fabrication process flow is depicted in Fig. 5 starting for a Y-cut LNOI 4" wafer purchased from a third party vendor [32]. The LN thin film (3" diameter and 500 nm in thickness) was bonded to Silicon dioxide (SiO_2, 1 μm thick) on an LN substrate using the smart cut technology [27] [see Fig. 5(a)]. The first step is the lift-off of evaporated Al thin film [see Fig. 5(b)] which is 100 nm thick. After this step, 400 nm Au layer lift-off is performed [see Fig. 5(c)] for coating the Al pads and make them mechanically more resilient to probe landing. The next step is the deposition of SiO_2 (1 μm thick) [see Fig. 5(d)], which is used as a mask layer during the LN etch. Chromium (Cr) (50 nm thick) is then deposited [see Fig. 5(e)] and used as a mask for etching SiO_2. This Cr layer is patterned twice. The first pattern is generated with optical lithography to define the waveguides (WGs) and the racetrack [see Fig. 5(f)]. The second Cr patterning is performed at the die level using electron-beam lithography to define the gratings couplers [see Fig. 5(g)]. Then SiO_2 is etched in an RIE process using fluorine-based chemistry with a Cr mask [see Fig. 5(h)]. Chlorine-based chemistry is used in an ICP process to partially etch the LN with the SiO_2 mask [see Fig. 5(i)]. The etch depth is controlled by timing so the actual target depth (330 nm) varied by $\pm$40 nm across the wafer. The variation is a function of the uniformity of the bonded thin film transferred and the uniformity of the etch. However, we do not expect such variations to cause significant changes in

TABLE 2
ICP RIE Recipe for Etching of Lithium Niobate

Parameter	**Value**
Pressure	5 mT
Cl_2 gas flow	25 sccm
BCl_3 gas flow	50 sccm
Ar gas flow	10 sccm
ICP power	600 W
RF power	250 W

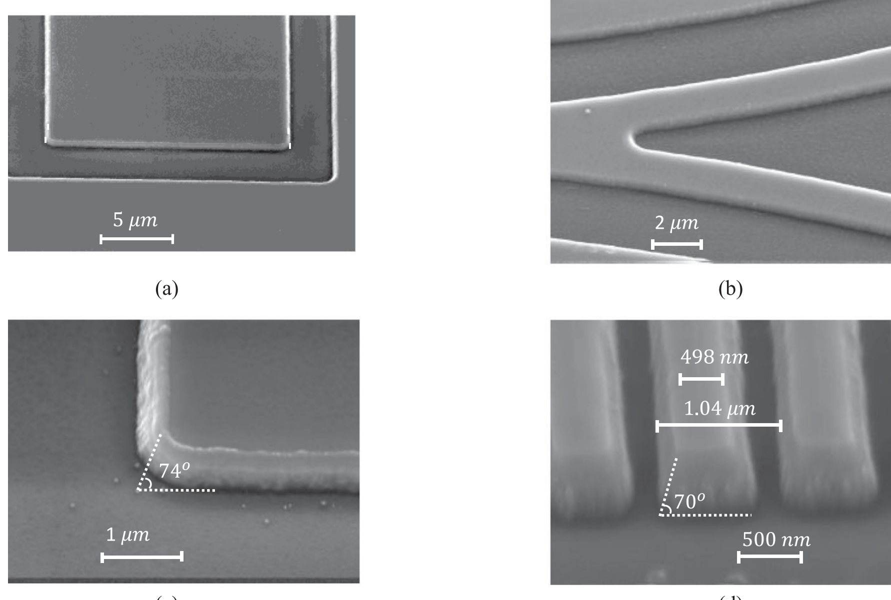

(a) (b) (c) (d)

Fig. 6. Various photonic components etched in LN with the same etch depth. a) Wide waveguide etched in LN. b) Y junction. c) Tilted view for the waveguide showing side wall angle measured as 74°. d) Tilted view for the gratings coupler showing side wall angle measured to be 70°.

the EO demonstration. The Cr mask is also removed during the ICP etch step. The final step is wet etch of SiO_2 using Al PAD etch [see Fig. 5(h)], which is meant to etch the SiO_2 film selectively with respect to the Al pads. The process parameters used for etching the LN are listed in Table 2. The selectivity between the LN and SiO_2 is found to be 1:2 and the etch rate is about 60 nm/min. Fig. 6 shows SEMs for various photonic components fabricated using the aforementioned process including LNOI waveguides, grating couplers and Y junctions. The tilted view shows a sidewall angle of 70° for the grating coupler and about 74° for the waveguides. The difference is due to the use of different resist layers for the definition of these features.

The fabricated device transfer function was measured using a tunable LASER source, SANTEC TLS 510. The device response is shown in Fig. 7 together with the fitting to Equation (4). The fitting gives values of $a^2 = 0.89$ and $r^2 = 0.81$, which correspond to an unloaded Q of 1.3×10^5, a loaded Q of about 48,000, and a propagation loss of about $\alpha = 2.3$ dB/cm. The extracted value for

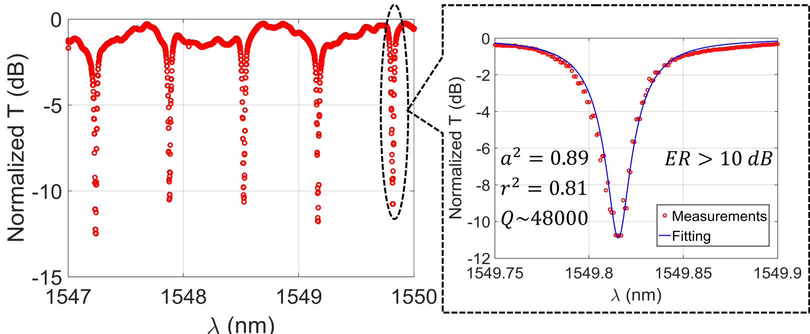

Fig. 7. Measured response for the RT EOM with a zoom-in view showing the fitting of a loaded Q of 48000.

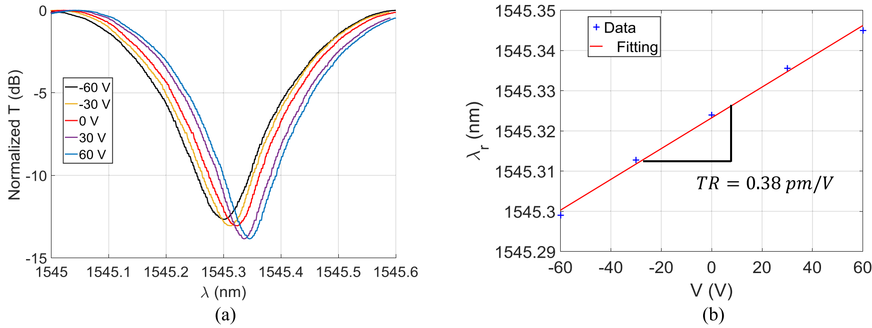

Fig. 8. Tuning of the resonance condition of the RT EOM by changing the applied DC voltage. a) Measured transfer function for the racetrack at different DC voltages. b) Resonance wavelength for the racetrack as function of the applied voltage.

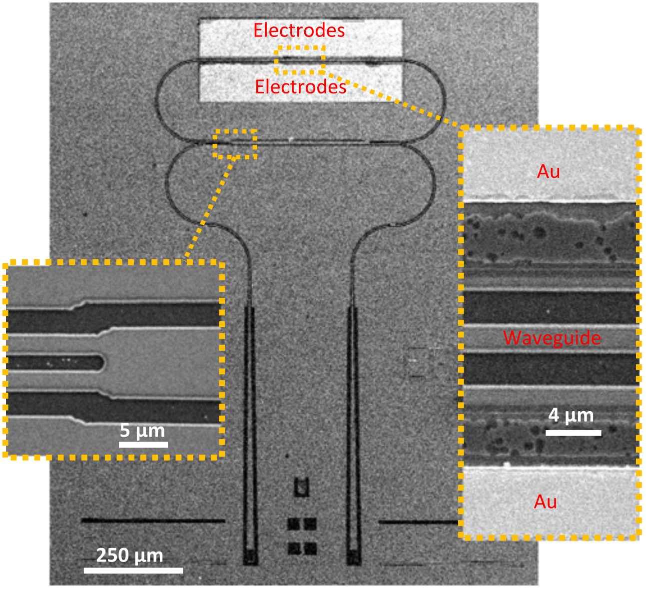

Fig. 9. SEM for the fabricated RT EOM.

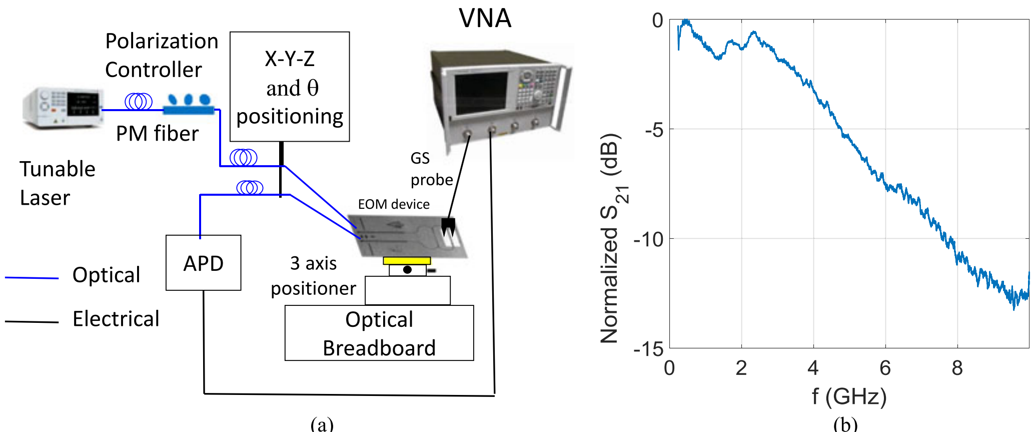

Fig. 10. (a) Optical setup for high speed modulation. (b) Measured S_{21} for the EOM.

$r^2 = 0.81$ is close to the design value, $r^2 = 0.83$, where the small discrepancy might be attributed to the losses at the coupling interface between the input (output) waveguide and the MMI waveguide. An ER larger than 10 dB was extracted given these coupling conditions.

Various values of DC voltages were applied on the EOM electrodes and a *TR* of 0.38 pm/V was measured (see Fig. 8). This is approximately 3x lower than the design value (1.1 pm/V). The difference might be related to the fact that Al was slightly attacked during the wet etch step of the SiO_2 as can be clearly seen in the SEM in Fig. 9. This implies that the electric field was applied across a larger separation, Δ. Assuming that the Al was completely attacked at the edges where there is no Au coverage, the theoretical *TR* can be re-evaluated as 0.61 pm/V, which is closer to the measured value. We attribute the remaining discrepancy to the material properties of the ion-sliced films.

High speed modulation was also tested for this device using the setup shown in Fig. 10(a). A vector network analyzer (VNA) was used to measure the scattering parameter, S_{21}, of the device. Port 1 of the VNA is used to apply the electrical modulation signal using a GS probe. Port 2 is used to monitor the output of a 1544 New Focus avalanche photodetector (APD) connected to the output gratings of the racetrack modulator. The measured 3-dB bandwidth is about 4 GHz and is limited mainly by photon lifetime inside the racetrack resonator.

4. Conclusion

In conclusion, a novel process for etching thin film of Y-cut LN using ICP-RIE was developed to fabricate a high performance EOM racetrack, a key element in reconfigurable photonic networks. A *TR* of 0.32 pm/V, modulation bandwidth of 4 GHz and *ER* larger than 10 dB were experimentally demonstrated. A butterfly MMI coupler in LN was also introduced for the first time, and enabled achieving critical coupling conditions. For the first time, the propagation loss of etched waveguides in Y-cut LNOI films were estimated. The measured propagation loss and unloaded Q of the racetrack resonator clearly prove that the etching method and proposed LNOI platform are a very interesting solution for integrated photonic components.

Acknowledgment

Any opinions, findings, and conclusions or recommendations expressed in this publication are those of the author(s) and do not necessarily reflect the views of DARPA.

References

[1] Q. Xu, B. Schmidt, S. Pradhan, and M. Lipson, "Micrometre-scale silicon electro-optic modulator," *Nature*, vol. 435, no. 7040, pp. 325–327, May 2005.
[2] D. Ding *et al.*, "Multidimensional purcell effect in an ytterbium-doped ring resonator," *Nat. Photonics*, vol. 10, no. 6, pp. 385–388, Jun. 2016.
[3] S. Ghosh and G. Piazza, "Laterally vibrating resonator based elasto-optic modulation in aluminum nitride," *APL Photon.*, vol. 1, no. 3, 2016, Art. no. 036101.
[4] A. Ksendzov and Y. Lin, "Integrated optics ring-resonator sensors for protein detection," *Opt. Lett.*, vol. 30, no. 24, pp. 3344–3346, Dec. 2005.
[5] A. Guarino, G. Poberaj, D. Rezzonico, R. Degl'Innocenti, and P. Günter, "Electro–optically tunable microring resonators in lithium niobate," *Nat. Photon.*, vol. 1, no. 7, pp. 407–410, Jul. 2007.
[6] G. T. Reed, G. Mashanovich, F. Y. Gardes, and D. J. Thomson, "Silicon optical modulators," *Nat. Photon.*, vol. 4, no. 8, pp. 518–526, Aug. 2010.
[7] P. Dumon *et al.*, "Low-loss SOI photonic wires and ring resonators fabricated with deep UV lithography," *IEEE Photon. Technol. Lett.*, vol. 16, no. 5, pp. 1328–1330, May 2004.
[8] X. Xiao, M. Li, L. Wang, D. Chen, Q. Yang, and S. Yu, "High speed silicon photonic modulators," in *Proc. Opt. Fiber Commun. Conf. Exhib.*, 2017, pp. 1–3.
[9] M. Garcia-Granda, H. Hu, J. Rodriguez-Garcia, and W. Sohler, "Design and fabrication of novel ridge guide modulators in lithium niobate," *J. Lightw. Technol.*, vol. 27, no. 24, pp. 5690–5697, Dec. 2009.
[10] H.-C. Huang, J. I. Dadap, G. Malladi, I. Kymissis, H. Bakhru, and R. M. Osgood, "Helium-ion-induced radiation damage in $LiNbO_3$ thin-film electro-optic modulators," *Opt. Exp.*, vol. 22, no. 16, pp. 19653–19661, Aug. 2014.
[11] A. J. Mercante, D. L. K. Eng, M. Konkol, P. Yao, S. Shi, and D. W. Prather, "Thin $LiNbO_3$ on insulator electro-optic modulator," *Opt. Lett.*, vol. 41, no. 5, pp. 867–869, Mar. 2016.
[12] H. Lu *et al.*, "Enhanced electro-optical lithium niobate photonic crystal wire waveguide on a smart-cut thin film," *Opt. Exp.*, vol. 20, no. 3, pp. 2974–2981, Jan. 2012.
[13] K. R. Parameswaran, R. K. Route, J. R. Kurz, R. V. Roussev, M. M. Fejer, and M. Fujimura, "Highly efficient second-harmonic generation in buried waveguides formed by annealed and reverse proton exchange in periodically poled lithium niobate," *Opt. Lett.*, vol. 27, no. 3, pp. 179–181, Feb. 2002.
[14] W. K. Burns, R. P. Moeller, C. H. Bulmer, and H. Yajima, "Optical waveguide channel branches in Ti-diffused $LiNbO_3$," *Appl. Opt.*, vol. 19, no. 17, pp. 2890–2896, Sep. 1980.
[15] M. L. Bortz and M. M. Fejer, "Annealed proton-exchanged $LiNbO_3$ waveguides," *Opt. Lett.*, vol. 16, no. 23, pp. 1844–1846, Dec. 1991.
[16] L. Cai, Y. Kang, and H. Hu, "Electric-optical property of the proton exchanged phase modulator in single-crystal lithium niobate thin film," *Opt. Exp.*, vol. 24, no. 5, pp. 4640–4647, Mar. 2016.
[17] G. Poberaj, H. Hu, W. Sohler, and P. Günter, "Lithium niobate on insulator (LNOI) for micro-photonic devices," *Laser Photon. Rev.*, vol. 6, no. 4, pp. 488–503, Jul. 2012.
[18] H. Hu, R. Ricken, and W. Sohler, "Lithium niobate photonic wires," *Opt. Exp.*, vol. 17, no. 26, pp. 24261–24268, Dec. 2009.
[19] R. Geiss *et al.*, "Fabrication of nanoscale lithium niobate waveguides for second-harmonic generation," *Opt. Lett.*, vol. 40, no. 12, pp. 2715–2718, Jun. 2015.
[20] A. Rao *et al.*, "Heterogeneous microring and Mach-Zehnder lithium niobate electro-optical modulators on silicon," in *Proc. Conf. Lasers Electro-Opt.*, 2015, pp. 1–2.
[21] M. Mahmoud, S. Ghosh, and G. Piazza, "Lithium niobate on insulator (LNOI) grating couplers," in *Proc. Conf. Lasers Electro-Opt.*, 2015, Paper SW4I.7.
[22] M. Mahmoud, C. Bottenfield, L. Cai, and G. Piazza, "Fully integrated lithium niobate electro-optic modulator based on asymmetric Mach-Zehnder interferometer etched in LNOI platform," in *Proc. IEEE Photon. Conf.*, 2017, pp. 223–224.
[23] L. Cai, S. Zhang, and H. Hu, "A compact photonic crystal micro-cavity on a single-mode lithium niobate photonic wire," *J. Opt.*, vol. 18, no. 3, 2016, Art. no. 035801.
[24] P. O. Weigel *et al.*, "Lightwave circuits in lithium niobate through hybrid waveguides with silicon photonics," *Sci. Rep.*, vol. 6, Mar. 2016, Art. no. 22301.
[25] L. Chen, M. G. Wood, and R. M. Reano, "12.5 pm/V hybrid silicon and lithium niobate optical microring resonator with integrated electrodes," *Opt. Exp.*, vol. 21, no. 22, pp. 27003–27010, Nov. 2013.
[26] C. Wang, M. Zhang, B. Stern, M. Lipson, and M. Loncar, "Nanophotonic lithium niobate electro-optic modulators," ArXiv: 170106470, Jan. 2017.
[27] J. J. Campbell and W. R. Jones, "A method for estimating optimal crystal cuts and propagation directions for excitation of piezoelectric surface waves," *IEEE Trans. Son. Ultrason.*, vol. 15, no. 4, pp. 209–217, Oct. 1968.
[28] A. Yariv, "Critical coupling and its control in optical waveguide-ring resonator systems," *IEEE Photon. Technol. Lett.*, vol. 14, no. 4, pp. 483–485, Apr. 2002.
[29] D.-X. Xu *et al.*, "High bandwidth SOI photonic wire ring resonators using MMI couplers," *Opt. Exp.*, vol. 15, no. 6, pp. 3149–3155, Mar. 2007.
[30] P. A. Besse, E. Gini, M. Bachmann, and H. Melchior, "New 2 times;2 and 1 times;3 multimode interference couplers with free selection of power splitting ratios," *J. Lightw. Technol.*, vol. 14, no. 10, pp. 2286–2293, Oct. 1996.
[31] M. Bachmann, P. A. Besse, and H. Melchior, "Overlapping-image multimode interference couplers with a reduced number of self-images for uniform and nonuniform power splitting," *Appl. Opt.*, vol. 34, no. 30, pp. 6898–6910, Oct. 1995.
[32] NANOLN JINAN Jingzheng 超平硅片 超平石英片.
[33] H. Bhugra and G. Piazza, "Lithium niobate in M/NEMS resonators," in *Piezoelectric MEMS Resonators*. New York, NY, USA: Springer-Verlag, 2017.